Journal of Materials Chemistry A

Accepted Manuscript

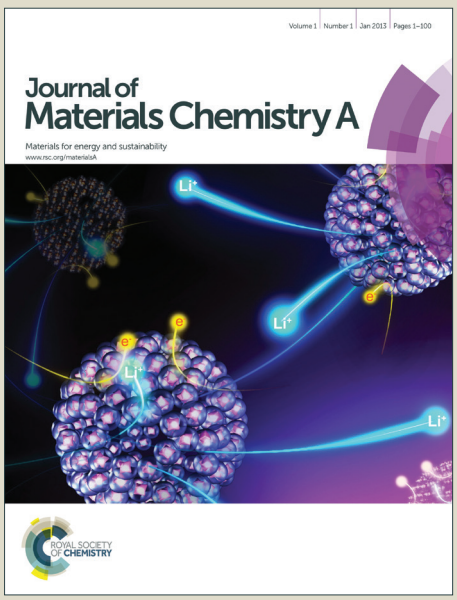

ROYAL SOCIETY OF CHEMISTRY

www.rsc.org/materialsA

Cite this: DOI: 10.1039/c0xx00000x

www.rsc.org/xxxxxx

ARTICLE TYPE

Synthesis of V_2O_5 Hierarchical Structures for Long Cycle-Life Lithium-Ion Storage

Guizhu Li,[1,2] Yuan Hou,[1] Hongfei Li,[1] Lisha Zhou,[1] Yongcai Qiu,[1,*] Hong Deng,[2,*] Yuegang Zhang,[1,*]

Received (in XXX, XXX) Xth XXXXXXXXX 20XX, Accepted Xth XXXXXXXXX 20XX
DOI: 10.1039/b000000x

A facile solvothermal method was used to synthesize V_2O_5 nanosheet hierarchical structures. Using different solvent systems, we obtained the hierarchical structures with different nanosheet thicknesses of <10 nm, 50-100 nm and 100-200 nm, respectively. A systematic investigation of their electrochemical properties showed that both the reversible lithium storage capacity and the cycling stability increased with the reduced thickness of nanosheets. In order to prevent the serious structural damage of the V_2O_5 electrodes during cycling, we employed a voltage-regulation charge/discharge scheme which led to a long cycle-life with an average capacity decay of 0.04% (2.0 to 3.0 V) and 0.10% per cycle (2.8 to 4.0 V) over 500 cycles.

Lithium-ion batteries (LIBs) have been widely used in portable electronic devices owing to their high energy density, long cycle life, no memory effect, and environment friendly features. [1-3] However, the development of new electronic devices and electric vehicles requires new-generation LIBs with substantial improvements in energy capacity, long lifespan, and rate capability.[4-6] This brings on a big challenge in developing new electrode materials for high performance LIBs.

Orthorhombic vanadium pentoxide (V_2O_5) is regarded as a very promising cathode material for next-generation LIBs due to its low cost and abundant resources, as well as good safety properties.[7, 8] However, the practical use of V_2O_5 as cathode materials for LIBs has been limited by its unstable cycling performance, poor electronic and ionic conductivity, and slow electrochemical kinetics.[9] To address these issues, electrode materials within nanometer-sized frameworks have been designed to provide a shorter conduction pathway for both electrons and Li ions, a larger electrode/electrolyte contact area, and a better accommodator for the strain induced by the Li-ion intercalation/deintercalation in nanomaterials.[10-12] To date, various nanostructures of V_2O_5, such as nanotubes,[13] nanowires,[14] nanofibers,[15] nanobelts, [16]nanorods,[17] and hollow spheres[18] have already been synthesized by a variety of methods, including sol–gel process, physical vapor deposition, electrospinning method, and hydrothermal treatment. With the unique electronic and mechanical properties of two-dimensional (2-D) nanomaterials, V_2O_5 nanosheets have recently received more and more attention.[19-21] Self-assembled hierarchical structures composed of V_2O_5 2-D building blocks have shown the merits of preventing agglomeration during electrochemical cycling and reducing interfacial contact resistance.[8, 19, 22-27] However, there is no report investigating the influence of the 2-D building blocks thickness on their electrochemical properties with respect to Li-ion storage. In addition, the cycling performance in the previous reports range from 50 to 100 cycles only, which is far from meeting the application requirements.

Herein, we report a facile solvothermal approach for large-scale synthesis of V_2O_5 nanosheet-nanoflower hierarchical structures. Urea as a morphology-controlling agent [28-30] was used to produce nanosheets. Using different solvent systems, we obtained hierarchical structures with different nanosheet thicknesses. The electrochemical Li-ion insertion/extraction investigation reveals that the hierarchical structures assembled from the thinnest nanosheets exhibit the highest specific capacity and best stability at high current rates. Furthermore, we employed a voltage-regulation charge/discharge scheme and achieved a highly stable capacity retention for over 500 cycles.

Experimental Section

Synthesis of V_2O_5 Hierarchical Structures. In a typical synthesis of V_2O_5 nanosheet precursor, 1 mmol urea (≧99%, was dissolved in a mixture of 3 mL of deionized (DI) water and 20 mL of ethylene glycol (EG,) in a 50 mL Teflon container, followed by the addition of 0.5 mmol Acetylacetone Vanadium(IV)Oxy Salt ($VO(CH_3COCH_2COCH_2)_2$, 99%). After stirring for 20 min, the container was sealed in a steel autoclave and kept in an electrical oven at 200°C for 12 h. The steel autoclave was cooled down naturally and the precipitate was collected by centrifugation and washed three times with pure ethanol. Urea with different dosage (0 mmol, 0.5 mmol, 2 mmol) was used to study its effect on the structures and morphologies of the V_2O_5 precursor hierarchical structures. Three different solvent systems, DI water/ethylene glycol (EG), DI water/isopropyl alcohol (IPA), and DI water/ethyl alcohol (ETA), were used to control the thickness of nanosheets (Table 1). The orthogonal V_2O_5 hierarchical structures were obtained by annealing of V_2O_5 precursors in air at 350 °C for 2 h with a heating rate of 1°C min^{-1}.

Table 1 Experimental Conditions for the Three Major V_2O_5 Hierarchical Structures

Precursor Sample #	Annealed Sample #	$VO(acac)_2$ (mmol)	Urea (mmol)	Reaction time	Solvent systems
P1	A1	0.5	1	12 h	DI water/EG
P2	A2	0.5	1	12 h	DI water/IPA
P3	A3	0.5	1	12 h	DI

					water/ETA

Materials Characterization. The morphologies of the V_2O_5 hierarchical structures were characterized using field emission scanning electron microscope (FESEM, S-4800) and transmission electron microscopy (TEM, Tecnai G2 F20 S-Twin). Thermogravimetric analysis (TGA, TG/DTA 6200) was carried out at a heating rate of 10 °C min^{-1} from room temperature to 500°C under air flow. Fourier Transform Infrared Spectroscopy (FTIR) spectroscopy measurement was performed using a Thermo FTIR spectrometer. The crystallographic information was collected by powder X-ray diffraction (XRD; Bruker, D8 AdvanceX-ray diffractometer, Cu Kα radiation, λ = 1.5406 Å). The specific surface areas were measured by a Brunauer–Emmett–Teller surface area analyzer (BET, Micromeritics ASAP2020).

Electrochemical Measurements. A working electrode was prepared by dispersing V_2O_5, carbon black (Super P), and a binder (sodium carboxyl methylcellulose (CMC) and styrene butadiene rubber (SBR) 1:1 by weight) with a weight ratio of 70:20:10 in ethanol/water (1:1 by volume) solution to from a slurry using an ultrasonicator. The slurry was spread on an aluminum foil and dried in a vacuum oven at 100°C for 12h. Half-cells were assembled using two-electrode Swagelok cells in an Ar-filled glovebox, with lithium foil as both the counter and reference electrodes. $LiPF_6$ (1.0 M) in ethylene carbonate/ethyl methyl carbonate/diethyl carbonate (EC/EMC/DEC, 20:65:15 v/v/v ratio) was used as the electrolyte. Cyclic voltammetry (CV; 2.0–4.0 V, 0.2 mV s^{-1}) measurements were performed on a VMP3 electrochemical working station. Galvanostatic charging/discharging was carried out using Land battery analyzers.

Results and discussion

The Hierarchical Structures of V_2O_5

V_2O_5-precursor hierarchical structures were synthesized via a template-free solvothermal method. A representative precursor sample (denoted as P1) was prepared in the DI water/EG solvent system, according to the experimental condition listed in the first row of Table 1. The XRD pattern of the as-synthesized sample P1, as shown in Figure 1a, can be assigned to a bipyramidal layered structure of V_2O_5 with the lattice parameters of a = 3.40257 Å, b = 11.24806 Å, c = 11.35478 Å, α = 92.1330, β = 88.1076, γ = 91.0732 (triclinic, space group *P*1).[16, 31]

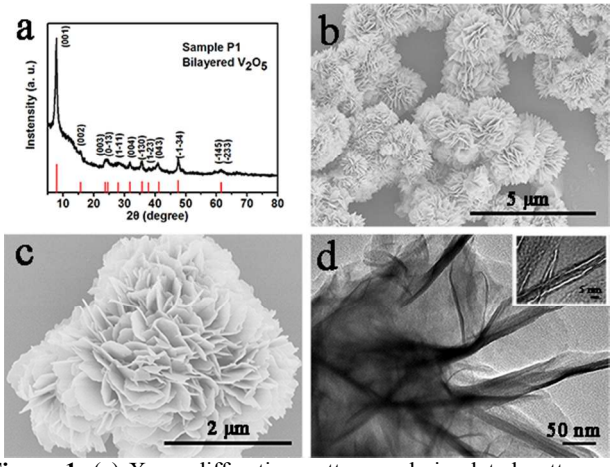

Figure 1. (a) X-ray diffraction pattern and simulated pattern of the as-prepared V_2O_5 precursor. (b, c) FESEM images, (d) TEM image of the bilayered V_2O_5 precursor sample P1 that was prepared according to the condition listed in Table 1.

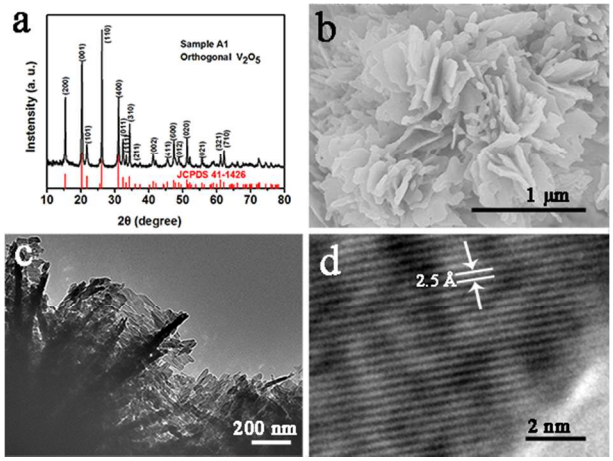

Figure 2. (a) XRD pattern of orthogonal V_2O_5 sample A1 obtained by annealing the sample P1, (b) FESEM image of sample A1, (c) TEM image of sample A1, (d) high-resolution TEM image of sample A1.

As shown in the low magnification FESEM image (Figure 1b), the sample P1 consists of flower-like hierarchical structures, with sizes ranging from 1.5 to 3 μm. The higher magnification FESEM image in Figure 1c shows that the "flower" is hierarchically assembled from numerous nanosheets. The nanosheets have smooth surfaces, as shown by the TEM images in Figure 1d, and their thickness is around 10 nm (Inset of Figure 1d).

The thermogravimetric analysis of the precursor sample P1 is carried out from 25 to 500°C at a heating rate of 10 °C min^{-1} in dry-air atmosphere (Figure S1). The weight loss below 170 °C corresponds to the loss of adsorbed water. The rapid weight loss above 175 °C is attributed to the decomposition of CO_3^{2-}, OH^- and ethylene glycol molecules that exist in the interlayer of bilayered V_2O_5. This assignment is also supported by the FTIR spectrum of the sample P1 (Figure S2). However, when the temperature reaches 322°C, the mass increases by 0.88%, which is probably due to the transformation of some low-valance vanadium oxides into V_2O_5. The sample weight remains stable after 350°C, which is the reason why we choose this temperature as the V_2O_5 annealing temperature in this study.

An orthogonal V_2O_5 hierarchical structure (denoted as A1 in Table 1) is obtained by annealing the precursor sample P1 in air at 350 °C for 2 h. The structure and morphology characterization results of A1 are shown in Figure 2. In Figure 2a, all major XRD peaks can be indexed to the orthogonal V_2O_5 phase (JCPDS card no. 41-1426, space group: Pmmn (59), a=11.516 Å, b=3.566 Å, c=3.777 Å).[32] The clean XRD pattern and the elemental analysis (Figure S3) indicate that a highly crystalline, pure orthogonal V_2O_5 phase is formed after thermal treatment at 350 °C. The original V_2O_5 precursor's flower-like hierarchical structure is well preserved without significant structural collapse after annealing (Figure 2b). But the nanosheet building blocks become rough and porous after annealing, as observed from a typical TEM image in Figure 2c. Figure 2d shows a selected area in the sample A1, where crystalline lattice fringes are observed. The lattice spacing of 2.50 Å corresponds to the (211) planes of orthogonal V_2O_5. The newly-formed hierarchical porous structure should be beneficial to enhancing the performance of Li-ion storage.[33-35]

The Morphological Evolution of V_2O_5 Precursors

To understand the V_2O_5 precursor morphology evolution during synthetic process, we investigated the morphologies from the samples obtained at different sovothermal reaction time. As shown in Figure 3a, the resulting precursor from 1 h reaction is composed of microspheres. When the reaction time extends to 2 h (Figure 3b), no microsphere remains and the sample is composed of nanosheets that are aggregated together. After solvothermal treatment for 3 h (Figure 3c), the carved sheets detach from the aggregates and begin to form irregular hierarchical structures. With a reaction time of 9 h, well-defined flower-like hierarchical structures are produced, as shown in Figure 3d. Further prolonging the reaction time to 12 h does not lead to any significant change in the morphology (Figure 1b).

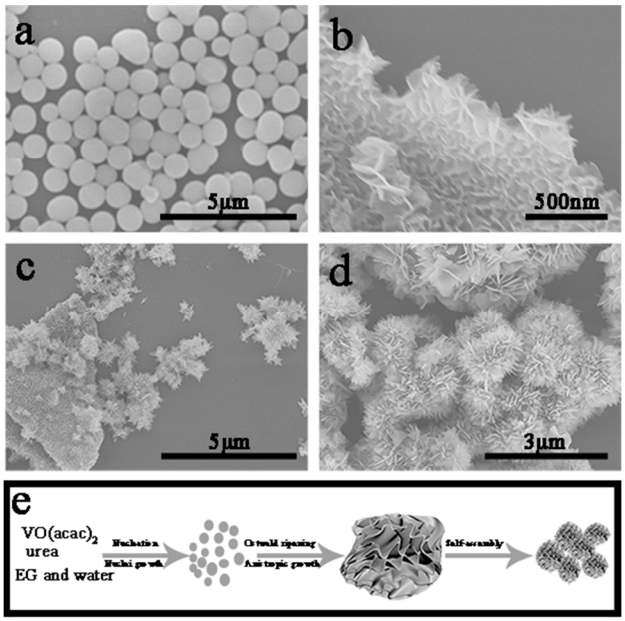

Figure 3. SEM images of the as-prepared V2O5 precursors collected at different reaction time: (a) 1 h, (b) 2 h, (c) 3 h, and (d) 9 h. (e) Schematic illustration of the morphological evolution process of the V_2O_5 precursor.

Based on the above experimental results, we propose a mechanism for the formation of flower-like hierarchical structure. In our experiment, EG and $VO(acac)_2$ can coordinate to each other via two hydroxyl groups and precipitate to become nuclei that quickly grow into the V-glycolate[36, 37] solid microspheres in isotropic growth directions.[38] As the reaction proceeds, Ostwald ripening causes the microspheres to aggregate, and more urea begins to decompose into CO_3^{2-} and NH_4^+, causing the intercalation of the CO_3^{2-} and/or NH_4^+ into the product. This results in the structure becoming strained and unstable. To release the strong stress and lower the total energy, the aggregates split into smaller nanosheets,[39] and the nanocrystals start to favor anistropic growth.[40] Then the nanosheets assemble to form flower-like hierarchical structure which may be caused by a combination of van der Waals forces, hydrogen bonds, and hydrophobic interactions in the solvothermal environment.[41-44] In summary, the conceivable growth process can be described as a fast nucleation of primary particles followed by aggregation and crystallization of primary particles. The possible formation mechanism of the products is illustrated in Figure 3e. This mechanism is also supported by our finding that the amount of urea plays an important role in the formation of sheet-like structures (Figure S4). Although the exact mechanism how urea tailors the morphology needs further investigation, the coordination effect between vanadium and urea or its decomposition products, such as CO_3^{2-}, NH_4^+, and OH^-, should be responsible for the initial seed crystallites to develop into nanosheets and finally grow into flower-like hierarchical structures.

The Influence of Solvent Systems on the thickness of nanosheets

Solvent system is an important factor in controlling the sizes and shapes of V_2O_5 hierarchical structures. As shown in Table 1, three different solvent systems were used to synthesize bilayered V_2O_5 precursors. Different from the flower-like hierarchical structure of sample P1 (Figure 1), the sample P2 obtained in the DI water/IPA solvent system shows a loosely-packed sphere-like hierarchical structure with a diameter around 1.5–3 μm (Figure 4a). The "spheres" consists of square nanosheets with a thickness of about 50–100 nm (Figure 4b). In the DI water/ETA solvent system (Sample P3), a densely-packed sphere-like hierarchical structure with a larger size of 2–5 μm is obtained (Figure 4c). The thickness of the nanosheets in the sample P3 is about 100–200 nm (Figure 4d), which is much thicker than that in the sample P1 and sample P2.

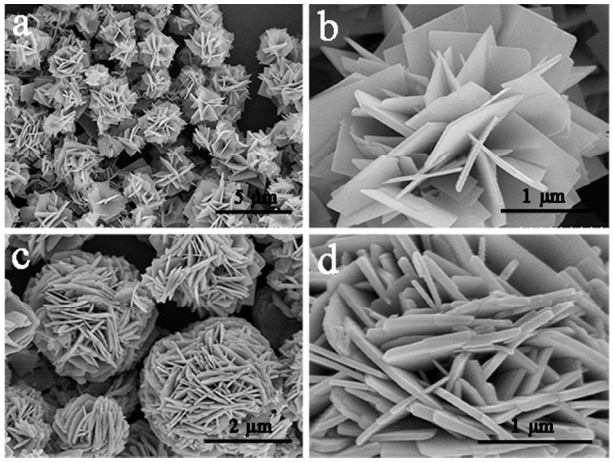

Figure 4. FESEM images of (a, b) microspheres consisting of square nanosheets with a thickness of about 50-100 nm in the DI water and IPA solvent system (Sample P2 in Table 1), (c, d) microspheres consisting of nanosheets with a thickness of about 100-200 nm in the DI water and ETA solvent systems (Sample P3 in Table 1).

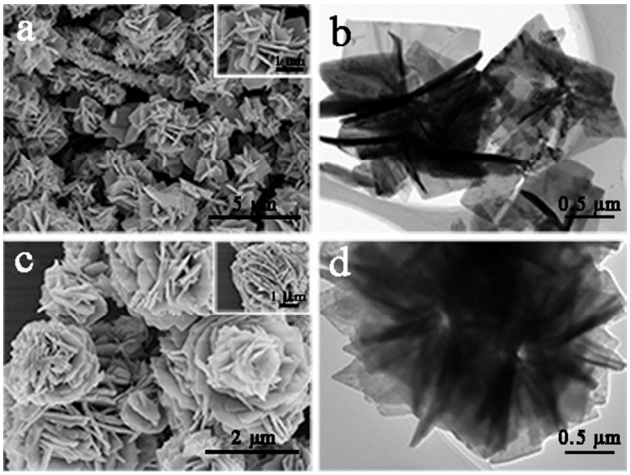

Figure 5. (a) FESEM images, and (b) TEM image of sample A2 obtained by annealing sample P2; (c) FESEM image, and (d) TEM image of sample A3 obtained by annealing sample P3.

Similar to the sample A1, orthogonal V_2O_5 hierarchical structures are obtained by annealing the sample P2 and P3 in air at 350 °C for 2 h. The annealed samples are denoted as sample A2 and A3, respectively. The XRD patterns of both samples agree well with the orthogonal V_2O_5 phase (JCPDS card no. 41-1426), which is the same as the sample A1 (Figure S5). As expected, there is not much change in the morphology after annealing. The sample A2 still maintains the loosely-packed sphere-like hierarchical structures (Figure 5a). The nanosheets in sample A2 is roughly twice thicker than that of sample A1. The TEM image shown in Figure 5b reveals that the nanosheets in A2 are square-shaped, with a length and width of about 1 μm. The morphology and structure of sample A3 are shown in Figure 5c, d. Similar to sample A2, there is no obvious change of morphology after annealing. However, the TEM images show that there is no cavity or porosity on the nanosheet surfaces of sample A2 and A3, which is different from the sample A1. This can be explained by that the nanosheets of sample A1 are very thin and the pores could be introduced by out-gasing of the micromolecules in the interlayer of bilayered V_2O_5 during the high temperature annealing process. The Brunauer−Emmett−Teller (BET) specific surface areas of the sample A1, A2 and A3 are measured to be 20.75, 18.50 and 4.35 $m^2 g^{-1}$, respectively (Figure S6).

The Electrochemical Performance

V_2O_5 is considered as one of the promising cathode materials for lithium-ion batteries, delivering a high theoretical capacity of 294 mA h g^{-1} based on the intercalation of two Li ions. [32] In recent years, 2D nanomaterials of transition-metal compounds, such as FeS,[45] VS_2, [46] and TiO_2 [47] have been actively studied as electrode materials in LIBs.[48] Similar to other 2D nanomaterials, very thin nanosheet structures may have a significant influence on the electrochemical performance of V_2O_5 nanomaterials. Here, the influence of the nanosheet thickness on the electrochemical properties of orthogonal V_2O_5 is investigated.

Figure 6a shows the first two consecutive CV curves for the electrodes prepared from the sample A1, A2, and A3, respectively, in the voltage range of 2.0-4.0 V vs Li/Li^+ with a scan rate of 0.2 mV s^{-1}. For the sample A1, the three cathodic peaks at the potentials of 3.31, 3.1 and 2.14 V indicate the multi-step Li-ion insertion processes of the active material, corresponding to the phase changes from α-V_2O_5 to ε-$Li_{0.5}V_2O_5$, then δ-LiV_2O_5, and finally γ-$Li_2V_2O_5$, respectively.[26] During the anodic scan, three peaks at 2.60, 3.27, and 3.46 V are clearly observed, which are attributed to the reverse reactions and the successive backward transformation of the phase from γ-$Li_2V_2O_5$ to δ-LiV_2O_5, ε-$Li_{0.5}V_2O_5$, and α-V_2O_5, respectively. The CV curve suggests a good reversibility of the electrode material. Despite of a slightly lower anodic peak intensity and a positive shift of the cathodic peaks, the CV curves for subsequent cycles are quite similar, suggesting a good stability of the electrodes. The other two samples have similar CVs indicating the sample A1, A2, and A3 share the same electrochemical reaction path.

Figure 6b shows the charge-discharge curves of 1st, 3rd and 5th cycles for the electrodes of the sample A1, sample A2 and sample A3 at a constant current density of 30 mA g^{-1} between 2.0 and 4.0 V vs Li/Li^+. In the first discharge curves, three typical plateaus at about 3.3, 3.1, and 2.2 V are observed in all three samples, which is good agreement with the CV results. The reversible processes are found in the following cycles.

Figure 6c shows rate capabilities of the cells made of sample A1, A2, and A3. The first discharge specific capacities are 300 mA h g^{-1}, 294 mA h g^{-1}, and 292 mA h g^{-1}, respectively, all of which are close to the theoretical specific capacity (294 mA h g^{-1}) of V_2O_5. Notably, the sample A1 shows an average specific capacity of ~ 293 mA h g^{-1} at a current rate of 30 mA g^{-1} (~ 0.1 C), ~ 275 mA h g^{-1} at a current rate of 60 mA g^{-1} (~0.2 C), ~254 mA h g^{-1} at a current rate of 150 mA g^{-1} (~0.5 C), ~232 mA h g^{-1} at a current rate of 300 mA g^{-1} (~1 C) , ~209 mA h g^{-1} at a current rate of 600 mA g^{-1} (~2 C), and when the current rate reverses back to 100 mA h g^{-1} at the 26th cycle, the capacity of the sample A1 recovers to 254 mA h g^{-1} and retains at 228 mA h g^{-1} after 80 cycles. These values are much higher than those of the sample A2 which are only ~262 mA h g^{-1} at 30 mA g^{-1}, ~230 mA h g^{-1} at 60 mA g^{-1}, ~206 mA g^{-1} at 150 mA g^{-1}, ~185 mA h g^{-1} at 300 mA g^{-1}, ~156 mA h g^{-1} at 600 mA g^{-1}, and picking up to ~206 mA h g^{-1} at 100 mA g^{-1}. Then it retains at 185 mA h g^{-1} after 80 cycles. The sample A3 shows the lowest discharge specific capacities of ~246 mA h g^{-1}, ~211 mA h g^{-1}, ~182 mA h g^{-1}, ~156 mA h g^{-1}, and 125 mA h g^{-1} at the current rates of 30, 60, 150, 300, 600 mA g^{-1}, respectively. When the current density decreases to 100 mA g^{-1}, the capacity of the sample A3 recovers to 178 mA h g^{-1} and retains at 132 mA h g^{-1} after 80 cycles. The results clearly show that the orthogonal V_2O_5 hierarchical structure consisted of the thinner nanosheets has the better electrochemical properties. This could be explained by that the thinner nanosheets could shorten the Li-ion diffusion length and the electron conduction path into the active materials[19] and reduce the volume change during the charge/discharge process. After 80 discharge/charge cycling performance test, the sample A1, A2 and A3 can still maintain their hierarchical structures (Figure S7). However, in contrast to the pristine samples, the nanosheets become thicker, especially for the sample A3. In addition, some nanosheets of the sample A3 are agglomerate, leading to a decrease of the voids in the hierarchical structure and therefore compromising the battery performance. This is demonstrated by the largest capacity degradation shown in Figure 6c. These results suggest that decreasing the thickness of the nanosheets can efficiently inhibit the volume change and aggregation of the V_2O_5 hierarchical structures and therefore retain their structured stability during during the charge/discharge process, as expected.

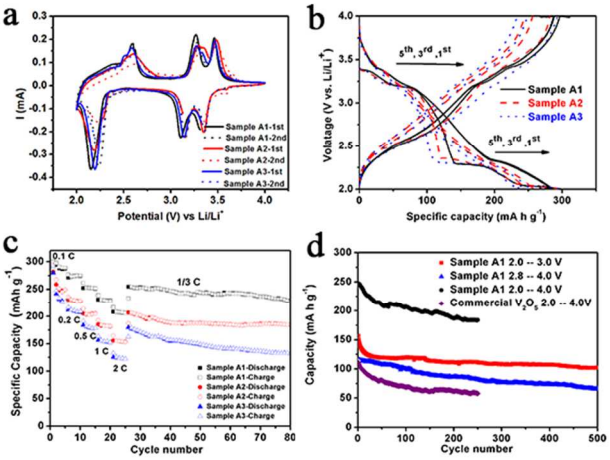

Figure 6. (a) Cyclic voltammograms of the orthogonal V_2O_5 sample A1, A2, and A3 for the first and second cycles. (b) Discharge/charge voltage profiles of the orthogonal V_2O_5 sample A1, A2, and A3 in the voltage range of 2–4 V vs. Li/Li^+ at a current density of 30 mA g^{-1} (c) Cycling performances of the sample A1, A2, and A3 at different current rates. (d) Cycling performances of the sample A1 in the voltage windows between

2.0 and 4.0 V (vs. Li^+/Li), between 2.0 and 3.0 V (vs. Li^+/Li), and between 2.8 and 4.0 V (vs. Li+/Li), and the commercial V_2O_5 between 2.0 and 4.0 V (vs. Li+/Li), respectively, cycled at a constant current density of 100 mA g^{-1}.

Further testing of the cycling stability was performed for the sample A1 and commercial V_2O_5 electrode at the current rate of 100 mA g^{-1} (Figure 6d). When a conventional voltage window of 2.0−4.0 V is applied, the sample A1 delivers a higher discharge capacity of 248 mA h g^{-1} at the first cycle and 184 after 250 cycles. For the commercial V_2O_5 electrode, the discharge capacity is only 111 mA h g^{-1} at the first cycle and 58 mA h g^{-1} at the 250th cycle. Despite of the significant improvement, the cycling stability of the sample A1 electrode is still not ideal considering a relatively high capacity decay rate of 0.11% per cycle. When the voltage window is regulated within the range of 2.0−3.0 V, however, except for an initial capacity drop from 157 mA h g^{-1} to 124.7 mA h g^{-1} after 20 cycles, the discharge capacity almost remaints stable to 102.6 mA h g^{-1} after 500 cycles, corresponding to a capacity decay rate of 0.04% per cycle. When the voltage window is regulated to 2.8−4.0 V, the sample A1 electrode also exhibits a very stable cycling performance. It delivers an initial capacity of 115.4 mA h g^{-1} at a current density of 100 mA g^{-1}, and retains a capacity of 65.8 mA h g^{-1} after 500 cycles, corresponding to a capacity decay of 0.09%. The similar phenomenon was also reported by other researchers.[7, 49-51] For example, Low *et al.* reported the change of voltage range from 2.0−4.0 V to 2.5−4.0 V, leading to a decrease of the capacity fading rate from 0.27% to 0.15% per cycle within 100 cycles. [49] Similarly, Zhang *et al.* reported a V_2O_5 hierarchical structure, showing the capacity retention of 80.5% after 250 cycles, corresponding to capacity decay rate of 0.08% per cycle.[45] However, to the best of our knowledge, there is no reported research on the cycling stability in the voltage window between 2.0 and 3.0V. Our work demonstrated here that the change of voltage window to 2.0−3.0V can effectively reduce the capacity decay as low as 0.04% per cycle within 500 cycles.

The effect of voltage regulation could be explained as the following: (1) The rapid capacity decay in the voltage ranges of 2.0 to 4.0 V may be caused by the huge volumetric and structural change of the electrode accompanying the multi-stage phase changes from α-V_2O_5 to ε-$Li_{0.5}V_2O_5$, then to δ-LiV_2O_5, and eventually to γ-$Li_2V_2O_5$. According to the previous theoretical investigation[52-54] , the first-stage Li-ion intercalation causes phase changes from α-V_2O_5 to ε-$Li_{0.5}V_2O_5$, then to δ-LiV_2O_5, corresponding to a voltage window from 4.0 to 2.8 V; and the subsequent Li-ion intercalation causes a phase change between δ-LiV_2O_5 and γ-$Li_2V_2O_5$, corresponding to a voltage window from 3.0 to 2.0 V. Since the unit cell volume of γ-$Li_2V_2O_5$ (a = 9.80 Å, b = 3.60 Å and c = 10.24 Å) is much larger than that of α-V_2O_5 (a = 11.51 Å, b = 3.56 Å and c = 4.37 Å), the phase changes will cause enormous structural destruction, resulting in a sharp capacity decay in the voltage ranges of 2.0 to 4.0 V. (2) The capacity fading in the voltage ranges of 2.0 to 3.0 V is only observed in the first several cycles. After these initial cycles, the reversible phase change only occurs between δ-LiV_2O_5 and γ-$Li_2V_2O_5$ within this voltage window. Because there is little difference between the unit cell volumes of δ-LiV_2O_5 (a= 11.24 Å, b=3.60 Å and c= 9.91Å) and γ-$Li_2V_2O_5$, the electrode structures are not much disrupted by the phase change. (3) It is highly possible that the first-stage Li-ion insertion/extraction process (2.0 − 3.0 V) is much more reversible than the second-stage Li-ion intercalation/deintercalation (2.8 − 4.0 V). Therefore, the phase transition from α-V_2O_5 to ε-$Li_{0.5}V_2O_5$, then to δ-LiV_2O_5 might not significantly disrupt the microstructure of the active materials.

Conclusions

In conclusion, a flower-like orthogonal V_2O_5 hierarchical structure was successfully synthesized by thermal transformation of a morphologically analogous precursor that is obtained through a facile solvothermal method in the presence of urea. The thickness of the nanosheet building blocks can be tailored by using different solvent systems (EG/DI Water: less than 10 nm, IPA/DI Water: 50-100 nm, ETA/DI Water: 100-200 nm). The electrochemical evaluation showed that the microstructures consisting of ultrathin V_2O_5 nanosheets with a thickness of ~10 nm exhibited the best Li-ion storage capacity and rate capability. When the voltage window was regulated between 2.0 and 3.0 V, the V_2O_5 material demonstrated stable cyclability (retained ~102 mA h g^{-1} after 500 cycles at 100 mA g^{-1}). We believe that structure-function relations revealed in this work could be applied to other electrode materials systems, help to improve the performance of Li-ion batteries.

This work was supported by the National Science Foundation for Post-doctoral Scientists of China (014M550314), the Natural Science Foundation of Jiangsu Province, China (BK20140383), Suzhou Science and Technology Development Program (ZXG2013002), and the National Natural Science Foundation of China (Grant No. 21303251, 21171060, 21403287, and 21433013).

Notes and references

[1]*i-Lab, Suzhou Institute of Nano-Tech and Nano-Bionics, Chinese Academy of Science, Suzhou, Jiangsu 215123, China*
[2]*School of Chemistry and Environment, South China Normal University, Guangzhou 510006, China,*CORRESPONDING AUTHOR E-mail: (ygzhang2012@sinano.ac.cn; dh@scnu.edu.cn)*

Electronic Supplementary Information (ESI) available: Other characterizations including TGA, FTIR, EDX, BET, and XRD data. See DOI: 10.1039/b000000x/

1. A. Manthiram, A. V. Murugan, A. Sarkar and T. Muraliganth, *Energy Environ. Sci.* , 2008, **1**, 621-638.
2. A. Manthiram, *J. Phys. Chem. Lett.*, 2011, **2**, 176-184.
3. A. Manthiram, Y. Fu and Y. S. Su, *Acc. Chem. Res.*, 2013, **46**, 1125-1134.
4. T. H. Kim, J. S. Park, S. K. Chang, S. Choi, J. H. Ryu and H.-K. Song, *Adv. Energy Mater.*, 2012, **2**, 860-872.
5. Y. Li, J. Yao, E. Uchaker, J. Yang, Y. Huang, M. Zhang and G. Cao, *Adv. Energy Mater.*, 2013, **3**, 1171-1175.
6. Y. C. Qiu, S. H. Yang, H. Deng, L. M. Jin and W. S. Li, J. Mater. Chem., 2010, 20, 4439-4444.
7. R. X. Yu, C. F. Zhang, Q. Meng, Z. X. Chen, H. K. Liu and Z. P. Guo, *ACS Appl. Mater. Interfaces*, 2013, **5**, 12394-12399.
8. C. Zhang, Z. Chen, Z. Guo and X. W. Lou, *Energy Environ. Sci.* , 2013, **6**, 974-978.
9. M. S. Whittingham, *Chem. Rev.*, 2004, **104**, 4271-4301.
10. Y. Shi, B. Guo, S. A. Corr, Q. Shi, Y.-S. Hu, K. R. Heier, L. Chen, R. Seshadri and G. D. Stucky, *Nano Lett.*, 2009, **9**, 4215-4220.
11. Y.-S. Hu, X. Liu, J.-O. Mueller, R. Schloegl, J. Maier and D. S. Su, *Angew. Chem. Int. Ed.*, 2009, **48**, 210-214.
12. P. G. Bruce, B. Scrosati and J. M. Tarascon, *Angew. Chem. Int. Ed.*, 2008, **47**, 2930-2946.
13. J. S. Bonso, A. Rahy, S. D. Perera, N. Nour, O. Seitz, Y. J. Chabal, K. J. Balkus, J. P. Ferraris and D. J. Yang, *J. Power Sources*, 2012, **203**, 227-232.
14. R. S. Chen, W. C. Wang, C. H. Chan, H. P. Hsu, L. C. Tien and

Y. J. Chen, *Nanoscale Res. Lett.*, 2013, **8**, 443.
15. G. Wee, H. Z. Soh, Y. L. Cheah, S. G. Mhaisalkar and M. Srinivasan, *J. Mater. Chem.*, 2010, **20**, 6720-6725.
16. D. Su and G. Wang, *ACS nano*, 2013, **7**, 11218-11226.
17. Y. Q. Wang, Z. C. Li, X. Sheng and Z. J. Zhang, *J. Chem. Phys.*, 2007, **126**, 164706.
18. M. Sasidharan, N. Gunawardhana, M. Yoshio and K. Nakashima, *J. Electrochem. Soc.*, 2012, **159**, A618-A621.
19. Q. An, Q. Wei, L. Mai, J. Fei, X. Xu, Y. Zhao, M. Yan, P. Zhang and S. Huang, *PCCP*, 2013, **15**, 16828-16833.
20. J. Feng, X. Sun, C. Wu, L. Peng, C. Lin, S. Hu, J. Yang and Y. Xie, *J. Am. Chem. Soc.*, 2011, **133**, 17832-17838.
21. J. Cheng, B. Wang, H. L. Xin, G. Yang, H. Cai, F. Nie and H. Huang, *J. Mater. Chem. A.,* 2013, 1, 10814-10820.
22. Z. R. Dai, Z. W. Pan and Z. L. Wang, *Adv. Funct. Mater.*, 2003, **13**, 9-24.
23. S. J. Han, B. C. Jang, T. Kim, S. M. Oh and T. Hyeon, *Adv. Funct. Mater.*, 2005, **15**, 1845-1850.
24. Y. C. Qiu, W. Chen and S. H. Yang, *J. Mater. Chem.*, 2010, **20**, 1001-1006.
25. Y. Tang, X. Rui, Y. Zhang, T. M. Lim, Z. Dong, H. H. Hng, X. Chen, Q. Yan and Z. Chen, *J. Mater. Chem. A.* , 2013, **1**, 82-88.
26. A. Q. Pan, H. B. Wu, L. Yu, T. Zhu and X. W. Lou, *ACS Appl. Mater. Interfaces*, 2012, **4**, 3874-3879.
27. Y. C. Qiu, G. L. Xu, K. Y. Yan, H. Sun, J. W. Xiao, S. H. Yang, S. G. Sun, L. M. Jin and H. Deng, *J. Mater. Chem.,* 2011, **21**, 6346-6353
28. Y. Li, C. Peng, L. Li and P. Rao, *J. Am. Ceram. Soc.*, 2014, **97**, 35-39.
29. S. Agarwala, W. L. Ong and G. W. Ho, *Science of Advanced Materials*, 2013, **5**, 1418-1426.
30. Y. C. Qiu, G. L. Xu, Q. Kuang, S. G. Sun and S. H. Yang, *Nano Res.*, 2012, **5**, 826-832.
31. S. Tepavcevic, H. Xiong, V. R. Stamenkovic, X. Zuo, M. Balasubramanian, V. B. Prakapenka, C. S. Johnson and T. Rajh, *ACS nano*, 2012, **6**, 530-538.
32. A. Pan, H. B. Wu, L. Yu and X. W. Lou, *Angew. Chem. Int. Ed.*, 2013, **52**, 2226-2230.
33. R. Song, H. Song, J. Zhou, X. Chen, B. Wu and H. Y. Yang, *J. Mater. Chem.*, 2012, **22**, 12369-12374.
34. J. Xiao, J. Zheng, X. Li, Y. Shao and J. G. Zhang, *Nanotechnology*, 2013, **24**, 424004.
35. H. Sun, M. Ahmad and J. Zhu, *Electrochim. Acta*, 2013, **89**, 199-205.
36. A. Pan, T. Zhu, H. B. Wu and X. W. Lou, *Chemistry*, 2013, **19**, 494-500.
37. Y. C. Qiu, W. Chen, S. H. Yang, B. Zhang, X. X. Zhang, Y. C. Zhong and K. S. Wong, *Cryst. Growth Des.*, 2010, **10**, 177-183.
38. R. Z. Liu, Y. Z. Zhao, R. X. Huang, Y. J. Zhao and H. P. Zhou, *Eur. J. Inorg. Chem.*, 2010, 4499-4505.
39. T. Xiao, Y. Tang, Z. Jia, D. Li, X. Hu, B. Li and L. Luo, *Nanotechnology*, 2009, **20**, 475603.
40. Q. Gao, A. Zhao, Z. Gan, W. Tao, D. Li, M. Zhang, H. Guo, D. Wang, H. Sun, R. Mao and E. Liu, *CrystEngComm*, 2012, **14**, 4834-4842.
41. R. Rajendran, R. Muralidharan, R. S. Gopalakrishnan, M. Chellamuthu, S. U. Ponnusamy and E. Manikandan, *Eur. J. Inorg. Chem.*, 2011, 5384-5389.
42. H. Colfen and M. Antonietti, *Angew. Chem. Int. Ed.*, 2005, **44**, 5576-5591.
43. H. Colfen and S. Mann, *Angew. Chem. Int. Ed.*2003, **42**, 2350-2365.
44. Y. Politi, T. Arad, E. Klein, S. Weiner and L. Addadi, *Science*, 2004, **306**, 1161-1164.
45. C. Xu, Y. Zeng, X. H. Rui, N. Xiao, J. X. Zhu, W. Y. Zhang, J. Chen, W. L. Liu, H. T. Tan, H. H. Hng and Q. Y. Yan, *ACS nano*, 2012, **6**, 4713-4721.
46. Y. Jing, Z. Zhou, C. R. Cabrera and Z. F. Chen, *J. Phys. Chem. C.* , 2013, **117**, 25409-25413.
47. Y. P. Tang, D. Q. Wu, S. Chen, F. Zhang, J. P. Jia and X. L. Feng, *Energy Environ. Sci.* , 2013, **6**, 2447-2451.
48. D. Rangappa, K. D. Murukanahally, T. Tomai, A. Unemoto and I. Honma, *Nano Lett.*, 2012, **12**, 1146-1151.
49. A. Q. Pan, H. B. Wu, L. Zhang and X. W. Lou, *Energy Environ. Sci.* , 2013, **6**, 1476-1479.
50. H. G. Wang, D. L. Ma, Y. Huang and X. B. Zhang, *Chem. Eur. J* , 2012, **18**, 8987-8993.
51. S. Wang, Z. Lu, D. Wang, C. Li, C. Chen and Y. Yin, *J. Mater. Chem.*, 2011, **21**, 6365-6369.
52. J. S. Braithwaite, C. R. A. Catlow, J. D. Gale and J. H. Harding, *Chem. Mater.*, 1999, **11**, 1990-1998.
53. X. Rocquefelte, F. Boucher, P. Gressier and G. Ouvrard, *Chem. Mater.*, 2003, **15**, 1812-1819.
54. C. Delmas, H. Cognacauradou, J. Cocciantelli, M. Menetrier and J. Doumerc, *Solid State Ionics*, 1994, **69**, 257-264.

SYNOPSIS TOC

The “flower-like” vanadium pentoxide hierarchical structure assembled from ultrathin nanosheets is a promising electrode material for high-rate and long-cycle-life lithium-ion batteries.